



Deposited via The University of Leeds.

White Rose Research Online URL for this paper:

<https://eprints.whiterose.ac.uk/id/eprint/82830/>

Version: Published Version

---

**Article:**

Lan, Z, Lai, X, Roberts, KJ et al. (2014) X-ray Topographic and Polarized Optical Microscopy Studies of Inversion Twinning in Sodium Chlorate Single Crystals Grown in the Presence of Sodium Dithionate Impurities. *Crystal Growth & Design*, 14 (11). 6084 - 6092. ISSN: 1528-7483

<https://doi.org/10.1021/cg5012428>

---

**Reuse**

Items deposited in White Rose Research Online are protected by copyright, with all rights reserved unless indicated otherwise. They may be downloaded and/or printed for private study, or other acts as permitted by national copyright laws. The publisher or other rights holders may allow further reproduction and re-use of the full text version. This is indicated by the licence information on the White Rose Research Online record for the item.

**Takedown**

If you consider content in White Rose Research Online to be in breach of UK law, please notify us by emailing [eprints@whiterose.ac.uk](mailto:eprints@whiterose.ac.uk) including the URL of the record and the reason for the withdrawal request.

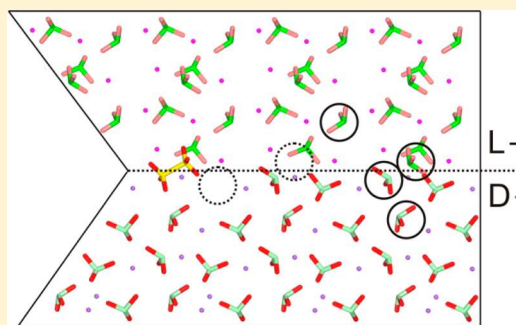
# X-ray Topographic and Polarized Optical Microscopy Studies of Inversion Twinning in Sodium Chlorate Single Crystals Grown in the Presence of Sodium Dithionate Impurities

Zhi-Peng Lan,<sup>#</sup> Xiaojun Lai,<sup>\*,#</sup> Kevin Roberts,<sup>#</sup> and Helmut Klapper<sup>§</sup>

<sup>#</sup>Institute of Particle Science and Engineering and Institute of Process Research and Development, School of Chemical and Process Engineering, University of Leeds, Leeds LS2 9JT, U.K.

<sup>§</sup>Institute of Crystallography, RWTH Aachen University, D-52056 Aachen, Germany

**ABSTRACT:** Sodium chlorate ( $\text{NaClO}_3$ ) crystallizes in the enantiomorphic space group  $P2_13$  which allows two chiral structural configurations (L and D forms). These crystals can form growth twins when the solution contains impurity ions of dithionate with the mole ratio 1:1000 (dithionate/chlorate) or higher. The impurity modifies the crystal habit from a cube-like morphology to one dominated by the minor  $\{111\}$  tetrahedral form. An X-ray topography study and the experimental observation of crystal growth reveal that the twinning phenomenon is consistent either as a result of the surface nucleation of a tetrahedral crystal of the morphologically opposite chirality on an existing tetrahedral habit face or by twinning at the nucleation stage and subsequent growth as two intergrown tetrahedral crystals. Polarized optical microscopy reveals that the optical activities of the twinned crystals observed are inverted with respect to each other. This is consistent with a merohedral mirror twinning system following twin law of  $m(001)$  (or identically  $\bar{1}$ ). Modeling of the crystal structure with respect to its external morphology is consistent with the dithionate impurity ions substituting for two adjacent chlorate ions at the twin boundary one from each of the contacting twin domains, through this creating a heterochiral twinned interface.



## 1. INTRODUCTION

Twinning in crystals has long been an exciting and interesting area for study among the mineralogy, crystallography, and industrial crystallization communities due to the special features associated with this phenomena, particularly the changes in morphology, variations in crystallographic symmetry, and production of mysterious structures. The twinning of sodium chlorate ( $\text{NaClO}_3$ ), generated in the presence of the habit-modifying additive sodium dithionate ( $\text{Na}_2\text{S}_2\text{O}_6$ ),<sup>1</sup> is a rare and interesting case that has not been experimentally characterized in detail in spite of the previous reports of its existence.

$\text{NaClO}_3$  crystallizes in an enantiomorphic point group 23 (space group  $P2_13$ ), representing the lowest symmetry of the cubic crystal class. This structure allows two chiral structural configurations producing potentially left-handed (L) and right-handed (D) morphological forms. In 1957 Ramachandran and Chandrasekaran<sup>2</sup> determined the absolute configuration of both D- and L- $\text{NaClO}_3$  crystals with respect to their optical rotatory properties. The polar growth habit of pure  $\text{NaClO}_3$ , comprising the  $\{001\}$ ,  $\{110\}$ , and  $\{111\}$  forms, has been predicted by Clydesdale et al.<sup>3</sup> employing a surface-specific attachment energy model based on the surface charges calculated from a combination of ab initio quantum mechanical calculations and interatomic potential parameters.<sup>4</sup>

$\text{NaClO}_3$  crystals grown from aqueous solution at moderate supersaturation exhibit the cubic faces of  $\{100\}$  type, which dominates the habit together with the much smaller rhomb-

dodecahedron  $\{110\}$ . In addition, the faster growing  $\{111\}$  and  $\{120\}$  forms can also be observed but only appear under very low solution supersaturations.<sup>1</sup> It should be noted, in this case, that due to the lack of any inversion or mirror symmetry the usual cubic octahedral  $\{111\}$  form is not a single form but two *symmetrically nonequivalent* and opposite  $\{111\}$  and  $\{\bar{1}\bar{1}\bar{1}\}$  tetrahedral forms. These forms are polar in nature, exhibit different surface chemistry, and hence behave differently with respect to their crystal growth and physical properties.<sup>1,5</sup> Every  $\text{NaClO}_3$  single crystal grown from pure solution exhibits only one of these tetrahedral forms;<sup>1,6</sup> i.e., a pure D-crystal comprises the major  $\{111\}_D$  type including four equivalent faces  $(111)_D$ ,  $(\bar{1}\bar{1}\bar{1})_D$ ,  $(\bar{1}\bar{1}\bar{1})_D$ , and  $(111)_D$  while a pure L-crystal comprises the major  $\{\bar{1}\bar{1}\bar{1}\}_L$  faces including  $(\bar{1}\bar{1}\bar{1})_L$ ,  $(111)_L$ ,  $(\bar{1}\bar{1}\bar{1})_L$ , and  $(111)_L$  (see Figure 1).<sup>1,5</sup> The structural chemistry underpinning this will be described later in section 3.1.

X-ray topography has been previously demonstrated to be an excellent technique for characterizing the growth-related defect structure of crystals. Early X-ray topographic studies of self-nucleated crystals of  $\text{NaClO}_3$  by Hooper et al.<sup>7</sup> explored the types of grown-in dislocations in  $\text{NaClO}_3$  crystals as well as their relationship to the crystal habit and growth mechanism. This systematic investigation examined the geometry of defects

Received: August 21, 2014

Revised: September 30, 2014

Published: October 1, 2014

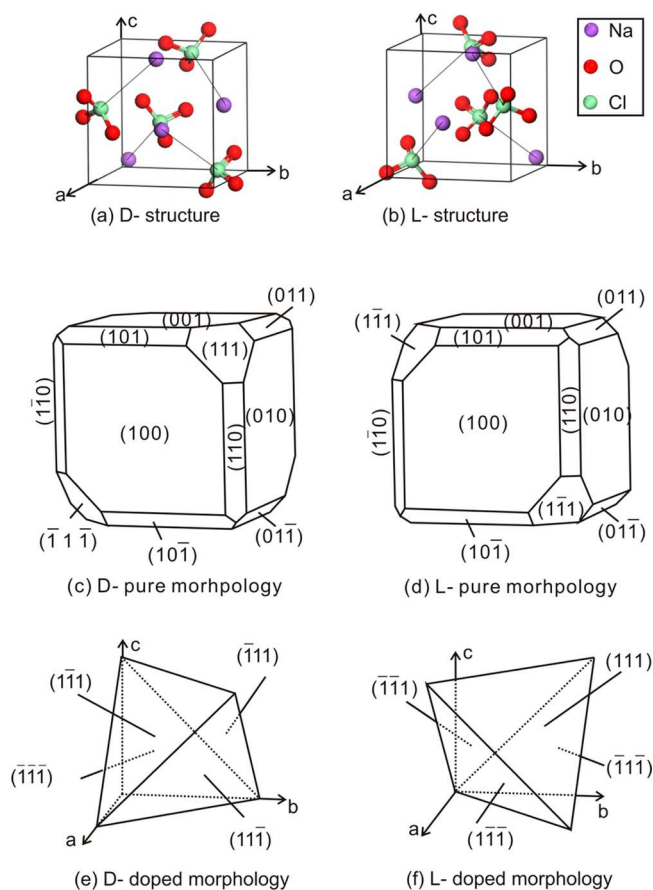


**Figure 1.** Interrelationship between the crystal chirality of  $\text{NaClO}_3$  and its external morphology: (a) D-structure; (b) L-structure. (c) Miller indices for habit faces of pure crystals with the D-structure. (d) Miller indices for the habit faces of pure crystals with the L-structure (after Clydesdale et al.<sup>3</sup>). (e) Miller indices for habit faces of doped crystals with the D-structure. (f) Miller indices for the habit faces of doped crystals with the L-structure.

in both crystals exhibiting the simple cubic habit  $\{100\}$  as well as those with the more complex habit with  $\{100\}$ ,  $\{110\}$ ,  $\{120\}$ , and  $\{111\}$  facets. In addition, the presence of postgrowth dislocation motion in  $\text{NaClO}_3$  in some crystals was reported to be caused by internal defects surrounded by stresses or mechanical damage in the external surface.<sup>8</sup> This technique has also been used to examine the influence of dislocations in  $\text{NaClO}_3$  on its solid-state reactivity.<sup>9</sup>

Buckley<sup>10</sup> systematically studied the habit modification of  $\text{NaClO}_3$  by the addition of  $\text{RO}_4^{2-}$  and related ions reporting the dithionate ion ( $\text{S}_2\text{O}_6^{2-}$ ) to be the most powerful additive in terms of enhancing the tetrahedral faces while suppressing the cubic ones. Ristic et al.<sup>1,5</sup> investigated the morphology and growth kinetics of  $\text{NaClO}_3$  in the presence of  $\text{S}_2\text{O}_6^{2-}$  impurities at varying concentration, where he considered all crystals to be D-type. At low  $\text{S}_2\text{O}_6^{2-}$  impurity concentration, the morphology of  $\text{NaClO}_3$  was found to have large  $\{100\}$  faces characterized by the appearance of small minor  $\{\bar{1}\bar{1}\bar{1}\}_D$  faces rather than the major  $\{111\}_D$  seen in pure crystals. This effect leads, in turn, to the formation of a tetrahedral rather than the more usual cubic morphology with increasing impurity concentration. According to Ristic et al.<sup>1</sup> the appearance of the minor  $\{\bar{1}\bar{1}\bar{1}\}_D$  forms is in contrast to the major tetrahedral  $\{111\}_D$  form which appeared as small facets during the growth from pure solution only. Ristic et al.<sup>1</sup> attributed the development of the minor  $\{\bar{1}\bar{1}\bar{1}\}_D$  forms at

the expense of the major tetrahedral form to the presence of  $\text{S}_2\text{O}_6^{2-}$  impurity, which was proposed to substitute for the  $\text{ClO}_3^-$  ions in the host lattice. This analysis was rationalized by the ionic geometry for the latter being similar to that of one of the  $\text{SO}_3$  subgroups of the  $\text{S}_2\text{O}_6^{2-}$  ion on these specific tetrahedral faces with the other subgroup protruding from crystal growth surface, blocking surface terrace motion and reducing the growth rate of these faces. Ristic et al.<sup>1</sup> also observed growth twins in  $\text{NaClO}_3$  which was attributed to an epitaxial relationship between the twin partners, induced by the  $(\text{SO}_3)_2^{2-}$  ions. However, so far there has not been any detailed experimental investigation to explore this phenomenon and validate the proposed model, and thus the detailed nature of the twinning behavior in this crystal system still remains unclear.

In this paper, a detailed study of the optical and defect properties associated with this impurity-induced twinning was carried out using polarized optical microscopy and X-ray topography. A key aim in this was to explore and characterize the twinning behavior associated and the lattice defects and, through this, understand the mechanism of twin formation and the structure of the twin boundary with respect to both the surface structure of  $\text{NaClO}_3$  and the ionic structure of the  $\text{S}_2\text{O}_6^{2-}$  impurity species.

## 2. EXPERIMENTAL SECTION

**2.1. Crystal Growth and Sample Preparation.** Single crystals of  $\text{NaClO}_3$  were grown from seeded supersaturated aqueous solutions in an agitated 500 mL temperature-controlled vessel. Heating was provided by an IR lamp source. A contact thermometer to a precision of  $\pm 0.1$  °C was used for temperature control. The seeds were prepared by solvent evaporation at room temperature in a 20 mL evaporation dish. Pure crystals were grown from pure  $\text{NaClO}_3$  aqueous solutions, and the doped crystals were grown from solutions containing defined amounts of  $\text{Na}_2\text{S}_2\text{O}_6$  (mole ratio,  $\text{S}_2\text{O}_6^{2-}/\text{ClO}_3^- = 1:1000$ ). In this, the seeded untwinned crystals were suspended from a fine thread within the vessel without contacting the crystallizer's internals. The growth solutions were initially saturated at 45 °C and thereafter slowly cooled to 25 °C at a cooling rate of about 1 °C per day.

A tungsten wire solvent saw, with water as solvent, was used to cut the as-grown crystals into crystal plates for subsequent analysis of polarized optical microscopy and X-ray topography. These were cut parallel to either the  $\{100\}$  planes for the pure crystals or the  $\{110\}$  crystal planes for the doped crystals. The surfaces of the cut plates were wet-polished, quickly rinsed, and dried with fine tissues. The final thickness of the crystal plates was about 1.5 mm.

**2.2. X-ray Topography.** The crystal growth defect structure, notably its twinning behavior, of the as-grown crystals was characterized by X-ray topography using a transmission Lang camera<sup>11</sup> with molybdenum  $K\alpha$ -radiation. The technical details and various applications are given, for example, by Tanner<sup>12</sup> and Lang<sup>13</sup> and in the case of twinned crystals by Klapper et al.<sup>14,15</sup> and Docherty et al.<sup>16</sup>

The linear absorption coefficient ( $\mu_o$ ) of  $\text{NaClO}_3$  for Mo- $K\alpha$  radiation was  $\mu_o = 1.25 \text{ mm}^{-1}$ , corresponding to a value of  $\mu_o t$  of ca. 1.9 resulting in an X-ray transmission factor of about 15% for a plate with a thickness ( $t$ ) of about 1.5 mm. The transmission topographs were recorded with fine-grained Agfa Structurix D4 X-ray film using the 002 reflection. This reflection has a sufficiently large structure factor moduli to provide the optimal combination for the spatial resolution and topographic contrast of crystal defects and a reasonably short exposure time.

**2.3. Polarized Optical Microscopy.** A transmission polarized optical microscope system was used comprising a light source, two polarizing media and a high-resolution camera. The crystal plates were placed between the two polarizers at the initial crossed position where their polarization directions are perpendicular to each other. With this polarization setup crystals with opposite optical activities appear in

different colors and thus can easily be recognized. Since  $\text{NaClO}_3$  crystallizes in a cubic crystal structure which is not of birefringence, its optical rotation power is independent of the direction of the light beam (isotropy). The latter applies to any orientation of the sodium chlorate crystals placed in between the polarizers. Thus, in this case, optical activity of the crystal was identified by rotating the top polarizer from the crossed position while observing the sequences of transmitted colors in the resultant crystal image. In this, the change of color in the order of blue, violet, and yellow for a clockwise rotation indicates the crystal to be in a dextrorotary ( $D^-$ ) state,<sup>17</sup> while for the levorotary ( $L^-$ ) state, the same sequence of colors appears for an anticlockwise rotation.

### 3. RESULTS AND DISCUSSION

**3.1. Structures and Morphology of the  $D^-$  and  $L^-$  Enantiomers.** The allocation of Miller indices for an enantiomorphous system such as  $\text{NaClO}_3$ , based on the crystallographic structure and crystal surface chemistry associated with the chiralities of the two enantiomers, is essential. Figure 1a–d shows these unit cell for the two enantiomers together with their corresponding morphologies as observed for pure crystals.<sup>2,3</sup> Each unit cell contains four  $\text{NaClO}_3$  molecules with a symmetry axis of each  $\text{NaClO}_3$  parallel to one of the four 3-fold  $\langle 111 \rangle$  axes in the unit cell.

The polar morphology, represented by the  $\{111\}_D$  surfaces on the  $D^-$ -crystal and the  $\{\bar{1}\bar{1}\bar{1}\}_L$  surfaces on the  $L^-$ -crystal (Figure 1c,d), reflects the different packing structures of the two enantiomers. In the unit cell of the  $D^-$ -enantiomer (Figure 1a), the four  $\text{ClO}_3$  groups are aligned with respect to the 3-fold  $\langle 111 \rangle$  axis with each  $\text{O}_3$  group of the chlorate anion closer to one surface of  $\{111\}_D$  type, i.e.,  $(111)_D$ ,  $(\bar{1}\bar{1}\bar{1})_D$ ,  $(\bar{1}\bar{1}\bar{1})_D$ , and  $(\bar{1}\bar{1}\bar{1})_D$ , while the chlorine atom of chlorate anion being closer to the geometrically opposite surfaces. This different surface chemistry of these polar faces causes the appearance of  $\{111\}_D$  faces on the final habit but not the  $\{\bar{1}\bar{1}\bar{1}\}_D$  faces.<sup>1</sup> Contrarily, for the  $L^-$ -enantiomer each of the  $\text{O}_3$  group of the chlorate anions is positioned closer to one  $\{\bar{1}\bar{1}\bar{1}\}_L$  surface (Figure 1b) while the chlorine atom is closer to  $\{111\}_L$ , resulting in the appearance of  $\{\bar{1}\bar{1}\bar{1}\}_L$  faces on the final habit but not the  $\{111\}_L$ .

Because of this polar surface chemistry, the  $\{\bar{1}\bar{1}\bar{1}\}_D$  faces and the  $\{111\}_L$  faces can absorb the  $\text{S}_2\text{O}_6^{2-}$  ion impurities resulting in a retardation of their growth rates.<sup>1,5</sup> It is worth emphasizing that, although the morphology of pure  $D^-$  and  $L^-$ -crystals present different forms of  $\{111\}_D$  and  $\{\bar{1}\bar{1}\bar{1}\}_L$ , respectively, the faces that appear on the morphology of  $\text{S}_2\text{O}_6^{2-}$ -doped  $D^-$  and  $L^-$ -crystals are  $\{\bar{1}\bar{1}\bar{1}\}_D$  and  $\{111\}_L$  faces, respectively. This effect has been attributed to the structural similarity of a  $\text{SO}_3^-$  group within the  $\text{S}_2\text{O}_6^{2-}$  ion to that of the  $\text{ClO}_3^-$  ion, an observation supported by the fact that the dithionate ion is also the only known impurity which so far has been observed to cause twinning of the  $\text{NaClO}_3$  crystal.<sup>1,5</sup> The  $\text{S}_2\text{O}_6^{2-}$  ion consists of two trigonal pyramids of  $\text{SO}_3^-$  linked via the S–S bond, in a staggered conformation with the two  $\text{SO}_2^-$  groups rotated by 60 deg with respect to each other (Figure 2b,c). Each  $\text{SO}_3^-$  subgroup has a similar configuration to that of  $\text{ClO}_3^-$ , with the same overall charge of  $-1$  (Figure 2a,b).<sup>1,18,19</sup> Thus, the  $\text{SO}_3^-$  at one side of a  $\text{S}_2\text{O}_6^{2-}$  ion could be absorbed at the  $\text{ClO}_3^-$  site during the growth but only at the  $\{111\}_L$  and  $\{\bar{1}\bar{1}\bar{1}\}_D$  minor tetrahedral surfaces. The outward facing orientation with the oxygen atoms of  $\text{ClO}_3^-$  closer to the  $\{\bar{1}\bar{1}\bar{1}\}_L$  and  $\{111\}_D$  preclude adsorption on the major tetrahedral faces.<sup>1</sup>

Figure 3a shows a projection of the  $D^-$ - $\text{NaClO}_3$  structure onto the  $(\bar{1}\bar{1}\bar{0})$  plane, with two facets of the tetrahedral  $\{111\}_D$  type

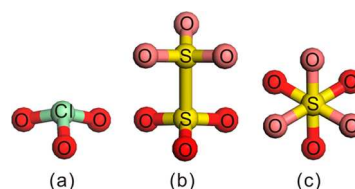


**Figure 2.** Atomic structures of the chlorate and dithionate ions. (a) Side view of  $\text{ClO}_3^-$  ion; (b) side view of  $\text{S}_2\text{O}_6^{2-}$  ion; (c) projection view of  $\text{S}_2\text{O}_6^{2-}$  ion along its S–S bond showing the ion's staggered conformation. Panels (a) and (b) show that the  $\text{ClO}_3^-$  and  $\text{SO}_3^-$  ionic groups have a similar stereochemistry.

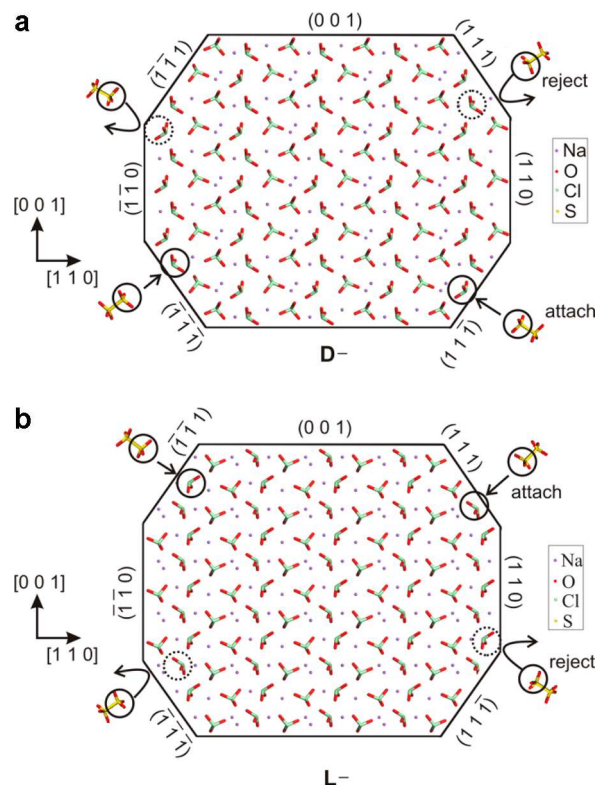


**Figure 3.** Projection of the  $\text{NaClO}_3$  structure along the  $[1\bar{1}\bar{0}]$  direction. (a)  $D^-$ -Structure with facets  $(111)_D$  and  $(\bar{1}\bar{1}\bar{1})_D$  (pointing inclined upward) of tetrahedron  $\{111\}_D$  and facets  $(\bar{1}\bar{1}\bar{1})_D$  and  $(\bar{1}\bar{1}\bar{1})_D$  (pointing inclined downward) of the opposite tetrahedron  $\{\bar{1}\bar{1}\bar{1}\}_D$ . (b)  $L^-$ -Structure with facets  $(111)_L$  and  $(\bar{1}\bar{1}\bar{1})_L$  (pointing upward) of tetrahedron  $\{111\}_L$  and facets  $(\bar{1}\bar{1}\bar{1})_L$  and  $(\bar{1}\bar{1}\bar{1})_L$  (pointing downward) of the opposite tetrahedron  $\{\bar{1}\bar{1}\bar{1}\}_L$ . Figure redrawn and adapted from Ristic et al. Copyright 1993 American Chemical Society.

(pointing inclined upward) and two facets of the tetrahedral  $\{\bar{1}\bar{1}\bar{1}\}_D$  type (pointing inclined downward). For the  $\{\bar{1}\bar{1}\bar{1}\}_D$  faces, the site of  $\text{ClO}_3^-$  with its pyramid apex pointing outward at the growing face (encircled with solid line) offers a nearly ideal location to absorb the  $\text{SO}_3^-$  of a  $\text{S}_2\text{O}_6^{2-}$  ion (also encircled with solid line). Once the  $\text{SO}_3^-$  is incorporated, the other  $\text{SO}_3^-$  of the  $\text{S}_2\text{O}_6^{2-}$  sticks out of the surface and hence can be expected to block surface terrace motion and hence slow down the growth rate of this face.<sup>1</sup> The opposite polar  $\{111\}_D$  faces would not be inhibited by docking  $\text{S}_2\text{O}_6^{2-}$  ions and hence would be expected to grow in relative terms faster and thus disappear from the final crystal habit. As outlined above, on the opposite tetrahedral facets of  $\{111\}_D$  type, the  $\text{ClO}_3^-$  pyramid apex pointing inward (encircled with dotted line) does not offer the correct stereochemistry for the whole  $\text{S}_2\text{O}_6^{2-}$  ion to be

easily incorporated. Therefore, the habit of the dithionate doped *D*-crystal becomes dominated by the minor tetrahedral faces of the  $\{\bar{1}\bar{1}\bar{1}\}_D$  type (Figure 1e).

Contrarily, by the same mechanism, for the *L*-enantiomer the tetrahedral faces capable of adsorbing the  $S_2O_6^{2-}$  ion would be the  $\{111\}_L$  faces, which is at the geometrically opposite direction compared to that of the *D*-enantiomer (Figure 3b). This results in the habit of doped *L*-crystal to be dominated by the tetrahedral faces of  $\{111\}_L$  type (Figure 1f).

**3.2. Growth of Crystals.** Large single crystals (e.g., with 20–40 mm of edge length) were readily grown from supersaturated aqueous solutions. In the absence of dopant and under moderate supersaturation, the morphology of the as-grown pure crystals was composed of the  $\{001\}$  and  $\{110\}$  faces (Figure 4a,b). The morphology of the doped crystal grown from the seed crystal, without twinning, presents a typical tetrahedral shape with slightly curved faces ( $\{\bar{1}\bar{1}\bar{1}\}$  and  $\{111\}_L$ ) and edges (Figure 4c,d). In occasional cases, a small second crystal was observed to form on an existing surface of the seeded crystal (Figure 4e,f). It exhibited a tetrahedral shape with its basal triangle rotated by  $60^\circ$  with respect to that of the seeded growing crystal. This was observed to grow and propagate into other existing surfaces, resulting in a tetrahedron on the top of the seeded growing crystal. Sometimes large twinned crystals (e.g., of 40 mm of side length or larger) were found to emerge at the bottom of the growth vessel due to unexpected self-nucleation (Figure 4g,h), rather than from the seeded grown crystals. They appeared to comprise two oppositely intergrown tetrahedra, occasionally with a small lens-shaped  $(001)_L$  facet on the curved  $[110]$  orientated edge on the top of one domain. Because of its contact with the bottom of the vessel, only the top half of the twinned crystal was observed to grow, whereas the growth of the lower half was inhibited by the constraints of the growth vessel. In Figure 4 it should be noted here that the Miller indices with subscripts are based on the determination of the optical properties of the crystals (see section 3.3). Overall, the morphology of these twinned crystals was found to be fully consistent with the observations of Ristic et al.<sup>1</sup> This behavior is illustrated schematically through the idealized morphology given in Figure 4i.

**3.3. Polarized Optical Microscopy.** Two crystal plates which were cut from the twinned crystal shown in Figure 4g were examined using polarized optical microscopy. The first plate (plate I) was cut parallel to the  $(110)$  plane so that the slice cut through the curved lens-shaped  $\langle 110 \rangle$  edge and hence through the center of the twinned crystal. As a result the plate contained the nucleation center of the crystal, and analysis of this permitted the growth history of the crystal to be tracked from the nucleation region through to the crystal's termination facets. The second plate (plate II) was cut from one of the remaining half crystal pieces, this time with the cut made normal to the plane of plate I and in doing so arranged to cut through its apex edge as well as intersecting the twinned crystal center. Both of these crystal plates were selected so that they would contain both of the twinned crystal domains.

Figures 5 and 6 show the resultant polarized optical micrographs recorded for plates I and II with the analyzer rotated by approximately  $20^\circ$  clockwise (a) and anticlockwise (b) respectively from the crossed polarizer position, revealing the levorotary (*L*-) and dextrorotary (*D*-) components of the twinned crystals with the colors being interchanged between

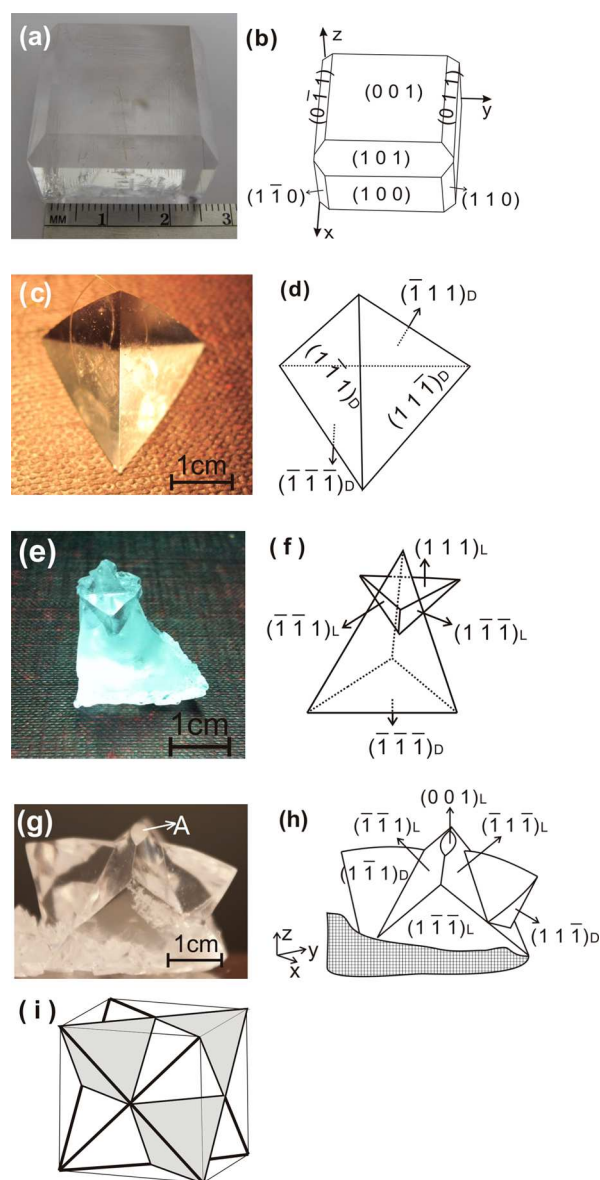


**Figure 4.** Experimental crystal morphologies of  $NaClO_3$  crystals prepared through seeded growth: (a) Photograph of a typical undoped crystal. (b) Sketch for the crystal in (a). (c) Photograph of an untwinned doped single crystal showing the typical tetrahedral morphology dominated by the  $\{\bar{1}\bar{1}\bar{1}\}_D$  form. (d) Sketch for the crystal in (c). (e) Photograph of a twinned doped single crystal with the second domain formed at the apex of the growing crystal. (f) Sketch for the crystal in (e). (g) Photograph of a twinned  $NaClO_3$  crystal showing two intergrown opposite tetrahedra with habit surfaces displaying slightly rounded faces and edges. On one of the  $\langle 110 \rangle$  edges, a lens-shaped  $(001)_L$  facet (labeled A) is visible. (h) Sketch for the crystal in (g). (i) Schematic showing an idealized morphology for an intergrowth twinned crystal.

the twin domains. For simplicity, these two domains are hereinafter referred as the *D*-domain and *L*-domain, respectively.

The twinned crystals were found to exhibit re-entrant edges at the outcrops where the twin boundaries intersect the crystal surface. The twin boundaries are formed by the path of the re-entrant edge during the growth process and thus have the character of a growth-sector boundary being roughly aligned close to the  $\{001\}$  plane which is the twin reflection plane referring to the twin law (e.g., Figure 5a,b; see section 3.5). The

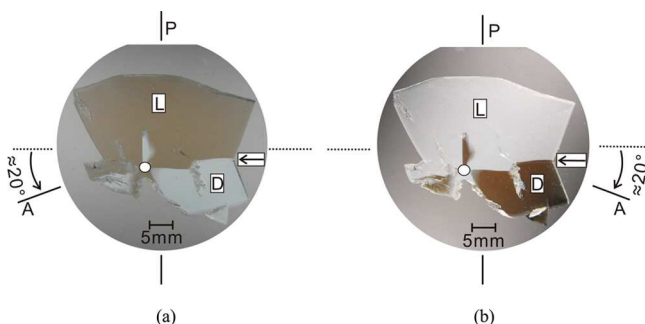


**Figure 5.** Photograph of plate I, cut parallel to  $(110)$ , of the twinned crystal as observed in polarized white light: (a) analyzer A rotated anticlockwise by about  $20^\circ$  from the crossed-polarizer position (dotted line); (b) analyzer A rotated clockwise by roughly the same angle with respect to the crossed-polarizer position (dotted line). For this angle the maximum optical contrast of the twin domains was found to be obtained. The white solid circle locates the origin of the self-nucleation site of the twinned crystal; the arrow indicates the position of the re-entrant edge; P shows the position of polarizer; A shows the position of the analyzer; L refers to the L-domain; D refers to the D-domain.

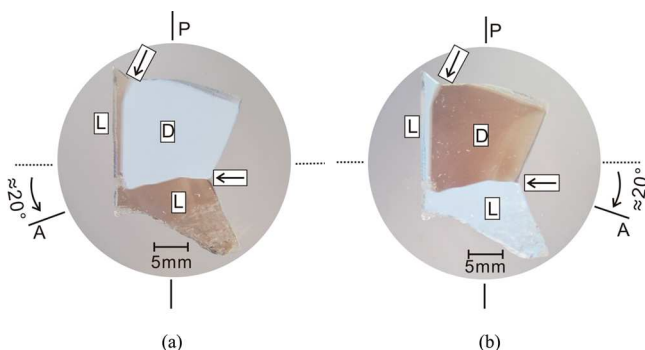


**Figure 6.** Photograph of plate II cut parallel to  $(110)$  of the twinned crystal in polarized white light: (a) analyzer A rotated anticlockwise by about  $20^\circ$  from the crossed-polarizer position (dotted line); (b) analyzer A rotated clockwise by roughly the same angle with respect to the crossed-polarizer position (dotted line). The left vertical edge of the plate reflects the position of the cut of plate I. All the data and labels are as described in Figure 5.

curved twinning interface reflects the varying ratio between the growth rates of the two interfacing twin domains. The twin boundaries and the twin domains were observed to converge into one point (white solid circle in Figures 5 and 6), which appears to be the origin of the twinning. Thus, the twinning can be considered to be initiated at the nucleation stage of the crystallization process. In Figure 5a, a small part of the D-domain is observed within the large L-domain reflecting the fact that the thickness of the plate contains a small volume portion of the D-domain crystal which had grown in the direction normal to the plate cut.

**3.4. X-ray Topography.** **3.4.1. Perfection of Undoped Crystals.** Figure 7a shows an X-ray topograph of a representative crystal plate  $(010)$  cut from an undoped crystal revealing the high perfection of the sample with very little strain contrast from the growth sectors and sector boundaries. This is consistent with the high perfection of these crystals with very low lattice ( $<10^{-4}$ ) strains induced by the growth process. However, two types of growth sectors, i.e.,  $\{001\}$  and  $\{101\}$ , can be deduced by the presence of the external habit faces, and

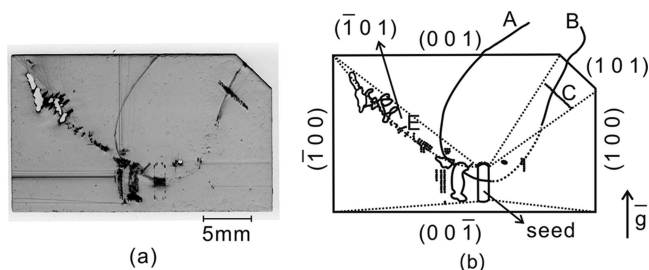


**Figure 7.** X-ray topograph of an  $(010)$  crystal plate of an undoped  $\text{NaClO}_3$  single crystal: (a) Reflection 002, Mo- $K\alpha$  radiation; (b) sketch of the principal features shown in (a) with the dotted straight lines representing the expected locations for growth sector boundaries. Note the trace of the seed support thread (AB) and the growth instability present in the  $(101)$  (C) and  $(\bar{1}01)$  (E) growth sectors. In the latter case, this is associated with rapid growth and the subsequent elimination of this growth sector from the external morphology.

these are summarized in the associated sketch, i.e., Figure 7b using dotted straight lines.

By observing the sources of the dislocation lines in both pure and doped crystals, it can be seen that most dislocations observed in the X-ray topographs were generated at inclusions, either at the seed/crystal interface or within inclusions generated through growth instabilities within the individual growth sectors. Another source of dislocations identified were those which were present in the seed crystals and which subsequently propagated into the growing crystal.

However, none of the dislocations present in the pure crystal were observed to be generated from any inclusions at the seed-crystal interface. This may be attributed to the much slower modulation of solution temperature during the regeneration process of the seed, which reduced the chance of producing dislocations at the inclusions.

**3.4.2. Perfection of Untwinned Doped Crystals.** Figure 8a shows an X-ray topograph as taken from an  $(\bar{1}10)$  plate cut

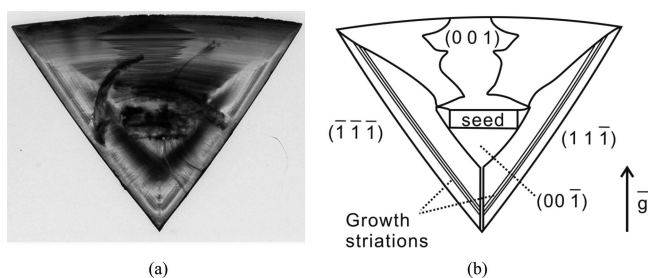


**Figure 8.** X-ray topograph of  $(\bar{1}10)$  plate cut from doped but untwinned single crystal: (a) Reflection 002, Mo- $K\alpha$  radiation; (b) sketch of the principle features identified from the topography shown in (a) showing the location of growth sectors and growth striations.

from the center of an untwinned single crystal (i.e., that shown in uncut form in Figure 4c) together with a schematic sketch (Figure 8b) highlighting the main features shown. It is interesting to note the comparatively high crystal perfection of this doped crystal, notably revealing surprisingly few dislocations together with contrast due to growth striations in parallel to the  $\{\bar{1}11\}$  type growth sector surfaces. Such striations are usually referred to as being caused by nonuniform impurity incorporation and/or structural perturbations at the growing front. Also striking is the slight curvature of the growth front which is also evident from the external morphology of the

crystals (see Figure 4c). Such interfacial curvature is more usually associated with interfacial roughening, i.e., the loss of a coherent step/terrace mediated growth front. However, this does not appear to be the case here where the growth striations show the same curvature but, nonetheless, the associated perfection of the crystal remains quite high. Full characterization of the growth defect structure will follow in a separate paper.<sup>20</sup> These growth striations, which appeared intensively in the topograph, have, however, largely facilitated the identification of different growth sectors as well as their boundaries. For example, the growth sector boundaries among the  $(\bar{1}\bar{1}\bar{1})_D$ ,  $(\bar{1}\bar{1}\bar{1})_L$ , and  $(00\bar{1})_D$  sectors shown in Figure 8 can be judged by the sharp bending of the striations at the interfaces of the growth sectors.

**3.4.3. Perfection of Doped but Twinned Crystals.** A typical feature of most inversion twins is that their domain structure can *only* be visualized by dislocation contrast due to different reflected intensities if polar reflections, such as 111 and its nonequivalent opposite  $\bar{1}\bar{1}\bar{1}$ , are used. However, the intensities of these reflections are only sufficiently different if the anomalous scattering is strong. For the  $\text{NaClO}_3$ , this is not the case as the constituent Na, Cl, and O atoms using Mo  $K\alpha$  radiation exhibit negligible anomalous scattering, and thus the 111 and  $\bar{1}\bar{1}\bar{1}$  reflections have essentially equal intensities. In addition, X-ray contrast by a mutual misorientation of the domains does not occur when there is an exact lattice coincidence of the twin partners as is the case here, and thus X-ray topography is not a feasible technique to directly distinguish twin domains of different chiralities in  $\text{NaClO}_3$ . Nonetheless this technique is very useful for the assessment of the growth-related defects in the twinned crystal and to assist in the deduction their distribution within the twin domains.

Figures 9 and 10 show the topographs of plates I and II (cf. Figures 5 and 6) of the twinned crystal, together with

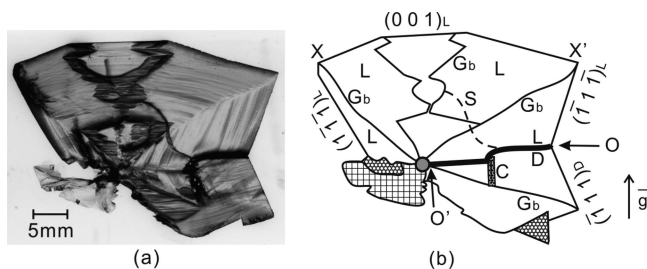


**Figure 9.** X-ray topograph of  $(110)$  plate I of the twinned crystal shown in Figure 4g: (a) reflection 002, Mo- $K\alpha$  radiation (cf. Figure 5). (b) Schematic illustration of growth sectors with their indices and twin domains. The upper margin  $X-X'$  of the plate corresponds to the rounded tetrahedral edge with the lens-shaped  $(001)_L$  facet shown in Figure 4g. Thick line  $O-O'$ : growth twin boundary;  $G_b$ : growth-sector boundaries between growth sectors; gray solid circle: nucleation region of the twinned crystal; C: row of liquid inclusions, the origin of dislocations; S: crack in the plate, merging into the twin boundary  $O-O'$ ; dark region at bottom left and bottom right: strongly disturbed part of crystal, partially out of reflection position;  $g$ : diffraction vector 002.

associated sketches which highlight the distribution of their defects and growth sectors. The presence of twinning can be easily recognized by the presence of the characteristic re-entrant edges and through the contrast of their associated twin boundaries. In this, it is noteworthy that the striations are more or less wavy, indicating the nonplanarity of the tetrahedral

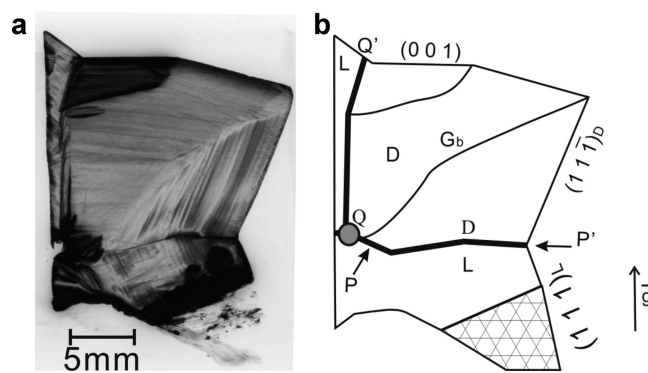


**Figure 10.** X-ray topograph of  $(\bar{1}\bar{1}\bar{0})$  plate II of the twinned crystal shown in Figure 4g: (a) reflection 002, Mo- $K\alpha$  radiation. (b) Schematic illustration of growth sectors with their indices and twin domains (cf. Figure 6). Thick lines  $P-P'$  and  $Q-Q'$ : twin boundaries; gray solid circle: nucleation region of the twinned crystal;  $G_b$ : growth-sector boundaries; hatched region at bottom right: strongly disturbed part of crystal;  $g$ : diffraction vector 002.

growth faces in each crystal domain. The sector boundaries are exhibited with the strong contrast between  $(001)_L$  and  $(111)_L$  type sectors or the trace of the sharp bends of the growth striations, mindful that the growth striations are parallel to the growing faces, respectively. An interesting feature revealed in Figure 9a, sketched in Figure 9b, is the small  $(001)_L$  growth sector which corresponds to the lens-shaped  $(001)_L$  facet shown in Figure 4g, which is embedded between two tetrahedral sectors. The associated sector boundaries are inclined with respect to the plate surface and therefore appear to be broad bands of strong contrast as a result of different perfection and slightly different lattice parameters between the  $\{111\}_L$  type and the  $(001)_L$  sectors. The irregular shape of the  $(001)_L$  sector exhibits its “growth history”, starting from the nucleation region of the crystal (gray circle) to the end of growth. After the development to a wide  $(001)_L$  sector from the growth origin, its facet had almost vanished due to a very fast growth for some period but then became wide again by the slowing down of its growth rate. It is not clear why the  $(001)_L$  facet, which is the dominant habit face of the pure crystal, appeared as a relatively larger facet in the doped twinned crystal, rather than in the doped untwinned single crystal (Figure 4c).

It is interesting that dislocations are not observed in all the growth sectors of the twinned crystal. Only a few dislocation lines are recognized in the  $(\bar{1}\bar{1}\bar{1})_D$  sector of D-domain and the  $(\bar{1}\bar{1}\bar{1})_L$  sector of L-domain (e.g., Figure 9a), and the  $(111)_L$  sector of L-domain (e.g., Figure 10a). These dislocations originate from highly imperfect regions (e.g., row C of inclusions in Figure 9a). The curved contrast line in Figure 9a, shown as dashed line and labeled S in Figure 9b, is a crack in the crystal plate. The hatched regions at the bottom parts of Figures 9b and 10b, showing no topographic contrast in their corresponding topographs, are strongly disturbed with pronounced mosaic character. They partially are out of X-ray reflection position due to their strong misorientation.

**3.5. Determination of Twin Law.** The observed growth twins exhibit two intergrown mutually inverted tetrahedra. Taking into account the cubic point symmetry 23 of the single crystal, the following two twin laws have the ability to generate this morphology.

(i) The 4-fold rotation by  $90^\circ$  (or  $270^\circ$ ) around any of the three cube axes  $\langle 100 \rangle$ . By group theory this is equivalent to  $180^\circ$  rotations around any of the diagonal cube directions  $\langle 110 \rangle$ . Any of these equivalent operations transform a tetrahedron into its opposite one, whereby the polarity of the 3-fold axes  $\langle 111 \rangle$  is inverted, but the chiral handedness is preserved. Since the optical rotation sense is inverted by the observed twinning of  $\text{NaClO}_3$ , this twin law has to be excluded from consideration.

(ii) The reflection across any of the cube planes  $\{001\}$ , which has, by equivalence, the same effect as an inversion, i.e.,  $\bar{1}$ . All these operations invert the tetrahedra and their polar axes as well as the chiral handedness and thus provide the correct twin law, which is defined as the set of all equivalent twin operations.<sup>22</sup> Thus, the observed twinning can be understood as a reflection twin across  $\{001\}$  as well as an inversion twin  $\bar{1}$ .

These two twin laws (i) and (ii) both exhibit another important property in that their twin operations belong to the maximum cubic symmetry group  $4/m\bar{3}2/m$ , mapping the lattices of the two twin partners upon each other. Thus, all lattice points of the two lattices coincide exactly, and so do their associated reciprocal lattice points. For X-ray diffraction this means that for any reflection both twin domains are always simultaneously in reflection position, and that in X-ray topography, i.e., analysis, both twin domains must be imaged together in a single diffraction image. This was in fact observed in this study as evidenced by Figures 9a and 10a. In the literature, these kinds of twins are referred to as “twinning by merohedry”<sup>21</sup> and “ $\Sigma 1$  twinning” (indicating the full coincidence of the lattices of the twin partners).<sup>22</sup>

**3.6. Origin of the Twinning Together with the Structure of Twin Boundary.** Though  $\text{NaClO}_3$  crystals have frequently been grown from pure aqueous solution, twins of any kind from pure growth solutions have never, to the authors' knowledge, been reported. This provides compelling evidence that the formation of the observed twinning was induced by the presence of the dithionate ions  $(\text{SO}_3)_2^{2-}$  in the doped crystallizing solutions. Such twins in  $\text{NaClO}_3$  could form, in principle, according to two different mechanisms, i.e., 2D surface nucleation at the dithionate site on a modified habit face<sup>1</sup> or dithionate-induced twinned 3D nucleation.

**3.6.1. Structural Model for Surface Nucleation.** Upon the incorporation, the half  $\text{S}_2\text{O}_6^{2-}$  ions that sticks out of the surface could create a local environment for  $\text{Na}^+$  and  $\text{ClO}_3^-$  ions to attach and hence to induce the surface (secondary) nucleation of the second twin domain of  $\text{NaClO}_3$ , i.e., in the opposite direction to the first domain (Figure 11).<sup>1</sup> It is worth emphasizing that, the density of the incorporated  $\text{S}_2\text{O}_6^{2-}$  ions may play an important role in mediating the nucleation process to take place. Because the configuration of the dithionate ion has a  $60^\circ$  rotation around the S–S bond between its two constituent  $\text{SO}_3^-$  groups (see Figure 2b,c), the opposite domain has a  $60^\circ$  rotation with respect to the first domain along the  $\langle 111 \rangle$  type axes, as observed in the twinned crystals received. Nevertheless, it should be noted that such heterochiral interface is only the interface where the twinning nucleated, but not the twin boundary which is formed by the path, during crystal growth process, of the re-entrant edges between adjacent  $\{111\}_D$  and  $\{1\bar{1}\bar{1}\}_L$  tetrahedral faces (see section 3.6.3).

**3.6.2. Structural Model for Bulk Nucleation.** Penetration or intergrowth twins from the nucleation center have been frequently observed (e.g., diamond by Machado et al.,<sup>23</sup> iron

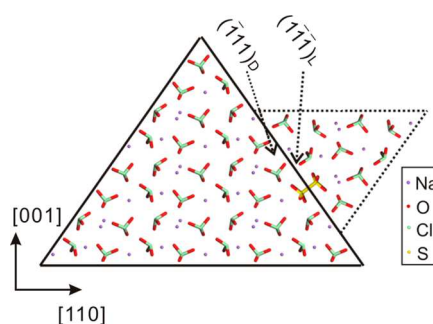


**Figure 11.** Projection of the structure of heterochiral interface for the surface nucleation twinning of  $\text{NaClO}_3$  along the  $[110]$  direction. On one tetrahedral surface of the D-crystal, the  $\text{S}_2\text{O}_6^{2-}$  ion (yellow and red in the figure) substitutes one  $\text{ClO}_3^-$  at the specific orientation of normal to the surface and through this induces the generation of the chiral opposite L-crystal.

borate by Diehl et al.<sup>24</sup> and lithium ammonium sulfate by Klapper<sup>14,16</sup>). The twinning mechanism due to their nucleation would result in the generation of macroscopic penetration twins.<sup>25</sup> In the case of  $\text{NaClO}_3$ , the presence of  $\text{S}_2\text{O}_6^{2-}$  anion impurity could act as a primary nucleating center facilitating the aggregation and binding of both L- and D-nuclei, and hence through this promoting the growth and development of the penetration twinned crystals. Although the surface-nucleation can induce the second twin domain which then grows over the edge of the first domain face onto the adjacent faces giving rise to the phenomenon of penetration twins (e.g., Figure 4e), this would not exclude the mechanism of the twin formation at the 3D nucleation stage, i.e., prior to crystal growth.

**3.6.3. Nature of the Twinning Interface.** The twin boundaries of the present twinned crystals are  $\{001\}$  cube planes, which are simultaneously the twin reflection planes. They are formed by the path, during growth, of the re-entrant edges between adjacent  $\{111\}_D$  and  $\{1\bar{1}\bar{1}\}_L$  tetrahedral faces. In this, the curved interface would represent a varying ratio between the respective growth rates of the twin domains, i.e., analogous to the path of the growth sector boundary. For the discussion of the atomic scale structure of this twin boundary and the influence of the dithionate ions, it is helpful to consider the conformation of the  $\text{ClO}_3^-$  ions on either side of the  $\{001\}$  interface between the  $\{111\}_D$  and  $\{1\bar{1}\bar{1}\}_L$  twinned growth sectors and their interaction with the dithionate  $\text{S}_2\text{O}_6^{2-}$  dopant.

Theoretically, for producing a twin boundary along  $\{001\}$  planes, there are two possible combinations of twin domains between the optical active structures, i.e., homochiral between D- & D- or L- & L-domains (related by twin law (i), i.e., by a  $90^\circ$  rotation around  $[001]$ , cf. Section 3.5) and heterochiral between D- & L-domains (related by twin law (ii), i.e., a reflection across  $\{001\}$ ). In both cases, the polarity of the  $\langle 111 \rangle$  symmetry axes is reversed during the twinning operation. Thus, at the  $\{001\}$  interface, the  $\text{ClO}_3^-$  ions are oppositely aligned across the domain boundary. For the D- & L-boundary the opposite  $\text{ClO}_3^-$  ions are rotated by  $60^\circ$  with respect to each other (Figures 12a,b and 13), which is consistent with the configuration of  $\text{S}_2\text{O}_6^{2-}$  (Figure 2b,c). However, for the D- & D- and L- & L- boundaries this angle is  $34.44^\circ$  (Figure 12c,d), which is different from the internal staggered angle of  $\text{S}_2\text{O}_6^{2-}$  ion; hence the  $\text{ClO}_3^-$  anions cannot stereochemically be substituted by an interface-bridging  $\text{S}_2\text{O}_6^{2-}$  anion. Therefore, only the D- to L-domain combination can provide the necessary geometry for the dithionate impurity to substitute a pair of

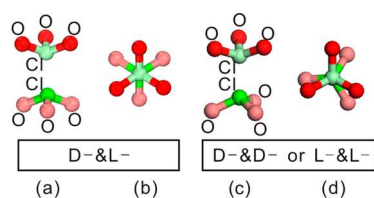


**Figure 12.** Schematic illustration of pair ions on the interface between twin domains. (a) Sideview of D- & L- combination. (b) Projection view of D- & L- combination. (c) Sideview of D- & D- or quivalent L- & L- combination. (d) Projection view of D- & D- or quivalent L- & L- combination.

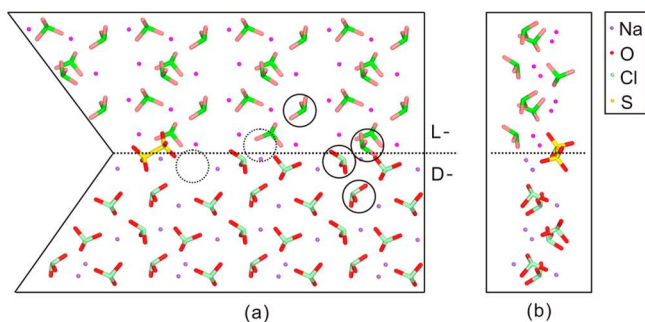


**Figure 13.** Projected views of the (001) twin boundary, where the  $S_2O_6^{2-}$  impurity is incorporated. (a) [110] projection of a  $S_2O_6^{2-}$  ion substituting one  $ClO_3^-$  from each domain, respectively. The lower is D-domain and the upper is L-domain. The S–S bond in  $S_2O_6^{2-}$  is colored in yellow. The ion orientation from the original structure of the heterochiral twin boundary is illustrated by solid circles, and the proposed modified structure of the twin boundary, after impurity incorporation, is illustrated by the dotted circles. (b) Projection normal to that in (a).

$ClO_3^-$  ions at the {001} twin boundaries and through this to structurally link the  $\{111\}_L$  growth sector with the  $\{\bar{1}\bar{1}\bar{1}\}_D$  growth sector (Figure 13). This analysis also suggests that homochiral twinning between D- & D- and L- & L- could not easily occur, even with the presence of  $S_2O_6^{2-}$ . The D- & L- model of twinning is consistent with the observations for both of the cases studied, i.e., twinning by 2D surface nucleation on an existing habit modified face or penetration twinning from 3D nucleation.

Following the surface incorporation mechanism,  $S_2O_6^{2-}$  can enter the (001) re-entrant edge through incorporation at the  $\{111\}_L$  or  $\{\bar{1}\bar{1}\bar{1}\}_D$  faces, where the pair of two oppositely aligned  $ClO_3^-$  ions from the D- and L-domains are substituted by the  $S_2O_6^{2-}$  (Figure 13). For dithionate incorporation at a twin boundary, there can be two  $S_2O_6^{2-}$  orientations with their S–S bonds normal to the  $\{111\}_L$  or  $\{\bar{1}\bar{1}\bar{1}\}_D$  faces respectively (e.g., see the two pairs of solid-circled  $ClO_3^-$  ions which are potentially substituted in Figure 13). However, only one of the two orientated pairs of  $ClO_3^-$  can be substituted at a twin boundary, because the substitution of the other orientated pairs by dithionate ions requires a horizontal displacement to the crystal lattice along the  $\langle 100 \rangle$  direction, which is not energetically preferred. The structural change caused by one of the two equivalent pairs can be understood in terms of the process of  $S_2O_6^{2-}$  incorporation at the re-entrant edge. In this, a local cavity will be created by excluding a  $ClO_3^-$  from its lattice site in the D-domain (e.g., see dot-circled  $ClO_3^-$  ions in Figure 13), due to the distance from the  $ClO_3^-$  to an oxygen of the  $S_2O_6^{2-}$  being too close. The paired  $ClO_3^-$  ions that are not

substituted by the  $S_2O_6^{2-}$  have their separation distance as close as 2.14 Å, but the oxygen of the  $ClO_3^-$  from L-domain would be too close to an existing  $ClO_3^-$  in the D-domain and hence could not coexist at the twin boundary. This would exclude the incorporation of one  $NaClO_3$  ion pair, thus resulting in a cavity in the L-domain (see dotted circle in Figure 13). Thus, in the imperfect twin boundary the  $S_2O_6^{2-}$  impurity ions could act as a bridge structurally linking the two domains together, thus leading to a reduction of the interfacial energy.

#### 4. CONCLUSIONS

Large single crystals of sodium chlorate doped with sodium dithionate have been prepared from seeded supersaturated solutions. The impurity addition was found to modify the growth habit from cube to tetrahedron, where the latter is consistent with the low cubic symmetry (point group 23) of this compound.

A combined polarized optical microscopy and X-ray topography study of doped crystals has been used to characterize the perfection and microstructure of these crystals. Growth sector mapping has identified the interrelationship between impurity doping and crystal perfection with the impurity incorporation producing more intense growth striations albeit with a surprisingly high degree of crystal perfection including a low dislocation content. At higher dopant levels, twinned crystals of both interpenetrating and surface nucleation twinning were observed. Characterization of these confirmed that this twinning case is merohedral in nature and is consistent with a twin law of  $m\{100\}$ , which is equivalent with the inversion  $\bar{1}$ . The twin boundary showed the salient features of growth boundaries, which, following analysis using both homochiral (L/L) or (D/D) and heterochiral (D/L) models based on the structural chemistry of the twinning interface, were found to be consistent with a heterochiral interface model. This proposed structural model suggests that the twin interface would be stabilized by the interfacial bridging impurity incorporated at the twin boundary, which is consistent with the mechanism for the formation and growth of the twinned crystals.

#### AUTHOR INFORMATION

##### Corresponding Author

\*Phone: +44 (0)113 3432439; e-mail: chexl@leeds.ac.uk.

##### Notes

The authors declare no competing financial interest.

#### ACKNOWLEDGMENTS

This work forms part of the doctoral studies<sup>6</sup> of one of us (Z.L.). Two of us (X.L. and K.J.R.) gratefully acknowledge the UK's EPSRC for their support in nucleation research at the Universities of Leeds and Manchester through their funding of the Critical Mass Project "Molecules, Clusters and Crystals" (Grant References EP/I014446/1 and EP/I013563/1, respectively).

#### REFERENCES

- (1) Ristic, R.; Sherwood, J. N.; Wojciechowski, K. Morphology and growth kinetics of large sodium chlorate crystals grown in the presence and absence of sodium dithionate impurity. *J. Phys. Chem.* **1993**, *107*, 10774–10782.
- (2) Ramachandran, G. N.; Chandrasekaran, K. S. The absolute configuration of sodium chlorate. *Acta Crystallogr.* **1957**, *10*, 671–675.

(3) Clydesdale, G.; Roberts, K. J.; Telfer, G. B.; Saunders, V. R.; Pugh, D.; Jackson, R. A.; Meenan, P. Prediction of the Polar Morphology of Sodium Chlorate Using a Surface-Specific Attachment Energy Model. *J. Phys. Chem. B* **1998**, *102*, 7044–7049.

(4) Telfer, G. B.; Gale, J. D.; Roberts, K. J.; Jackson, R. A.; Wilde, P. J.; Meenan, P. A Transferable Interatomic Potential for Alkali Chlorates and Bromates. *Acta Crystallogr. Sect. A Found. Crystallogr.* **1997**, *53*, 415–420.

(5) Ristic, R.; Shekunov, B. Y.; Sherwood, J. N. Growth of the tetrahedral faces of sodium chlorate crystals in the presence of dithionate impurity. *J. Cryst. Growth* **1994**, *139*, 336–343.

(6) Lan, Z. P. The Structural Role of Sodium Dithionate Impurity in the Habit Modification of Sodium Chlorate Single Crystals, Ph.D. Thesis, University of Leeds, 2014.

(7) Hooper, R. M.; Roberts, K. J.; Sherwood, J. N. X-ray topographic investigations of dislocations in sodium chlorate. *J. Mater. Sci.* **1983**, *18*, 81–88.

(8) Klapper, H. Defects in non-metal crystals. In *Characterization of Crystal Growth Defects by X-Ray Methods*; Tanner, B. K.; Bowen, D. K., Eds.; Plenum Press: New York, 1980; p 156.

(9) Begg, I. D.; Halfpenny, P. J.; Hooper, R. M.; Narang, R. S.; Roberts, K. J.; Sherwood, J. N. X-Ray Topographic Investigations of Solid State Reactions. I. Changes in Surface and Bulk Substructure During Incipient Thermal Decomposition in Sodium Chlorate Monocrystals. *Proc. R. Soc. A Math. Phys. Eng. Sci.* **1983**, *386*, 431–442.

(10) Buckley, H. E. The influence of  $\text{RO}_4$  and related ions on the crystallisation of sodium chlorate. *Z. Krist.* **1930**, *75*, 15–31.

(11) Lang, A. R. Topography. In *International Table for Crystallography*; Wiley: New York, 2006; Vol. C, pp 113–123.

(12) Tanner, B. K. *X-ray Diffraction Topography*; Pergamon Press: Oxford, 1976.

(13) Lang, A. R. Techniques and interpretation in X-ray topography. In *Diffraction and Imaging Techniques in Materials Science*; Amelinckx, S.; Gevers, R.; Van Landuyt, J., Eds.; Elsevier : Amsterdam, 1978; pp 623–714.

(14) Klapper, H. X-ray topography of twinned crystals. *Prog. Cryst. Growth Charact. Mater.* **1987**, *14*, 367–401.

(15) Klapper, H.; Hahn, T.; Chung, S. J. Optical, pyroelectric and X-ray topographic studies of twin domains and twin boundaries in  $\text{KLiSO}_4$ . *Acta Crystallogr. Sect. B Struct. Sci.* **1987**, *43*, 147–159.

(16) Docherty, R.; El-Korashy, A.; Jennissen, H.-D.; Klapper, H.; Roberts, K. J.; Scheffen-Lauenroth, T. Synchrotron Laue topography studies of pseudo-hexagonal twinning. *J. Appl. Crystallogr.* **1988**, *21*, 406–415.

(17) Bunn, C. *Chemical Crystallography*; Clarendon Press: Oxford, 1961; p 91.

(18) Abrahams, S. C.; Bernstein, J. L. Remeasurement of optically active  $\text{NaClO}_3$  and  $\text{NaBrO}_3$ . *Acta Crystallogr., Sect. B: Struct. Sci., Cryst. Eng. Mater.* **1977**, *33*, 3601–3604.

(19) Kirfel, A.; Will, G.; Weiss, A. X-ray diffraction study of  $\text{Na}_2\text{S}_2\text{O}_6 \cdot 2\text{H}_2\text{O}$  and  $\text{Na}_2\text{S}_2\text{O}_6 \cdot 2\text{D}_2\text{O}$ . *Acta Crystallogr., Sect. B: Struct. Sci., Cryst. Eng. Mater.* **1980**, *36*, 223–228.

(20) Lan, Z. P.; Lai, X.; Roberts, K. J.; Klapper, H. *J. Appl. Phys.* **2014**, in preparation.

(21) Catti, M.; Ferraris, G. Twinning by merohedry and X-ray crystal structure determination. *Acta Crystallogr., Sect. A* **1976**, *32*, 163–165.

(22) Hahn, T.; Klapper, H. Twinning of crystals. In *International Table for Crystallography*; Wiley: New York, 2006; Vol. D, pp 393–448.

(23) Machado, W. G.; Moore, M.; Yacoot, A. Twinning in Natural Diamond. II. Interpenetrant Cubes. *J. Appl. Crystallogr.* **1998**, *31*, 777–782.

(24) Diehl, R.; Jantz, W.; Nolaeng, B. I.; Wettling, W. Growth and properties of iron borate,  $\text{FeBO}_3$ . In *Currents Topics in Material Science*; Kaldis, E., Eds.; ECS: Pennington, NJ, 1984, *11*, 241–387.

(25) Senechal, M. The genesis of growth twins in crystals. *Sov. Phys.—Crystallogr.* **1980**, *25*, 520–524.